



Evolution and formation of North Atlantic Eighteen Degree Water in the Sargasso Sea from moored data



Xujing Jia Davis^{a,*}, Fiammetta Straneo^a, Young-Oh Kwon^a, Kathryn A. Kelly^b, John M. Toole^a

^a Physical Oceanography Department, Woods Hole Oceanographic Institution Woods Hole, MA 02543, United States

^b Applied Physics Laboratory, University of Washington, Seattle, WA 98195, United States

ARTICLE INFO

Available online 26 February 2013

Keywords:

North Atlantic Eighteen Degree Water
Formation mechanism
Air–sea heat flux
Lateral advection
Subsurface mooring measurements
Gulf Stream

ABSTRACT

Two profiling subsurface moorings were deployed as part of the CLIVar MOde Water Dynamics Experiment (CLIMODE) to study the formation and evolution of Eighteen Degree Water (EDW) from November 2006 to November 2007. Both moorings were deployed south of the Gulf Stream in the EDW outcrop region, the northwestern part of the subtropical gyre of the North Atlantic. The two moorings captured the seasonal evolution of EDW characterized by gradual mixed layer deepening and wintertime outcrop, rapid restratification from May to June and slower dissipation during the rest of the year. Superimposed on this seasonal cycle, the moored records are characterized by high frequency passing of eddies with a characteristic time scale of ~ 10 days, i.e. it took about 10 days for eddies to pass the mooring sites. The net impact of these eddy fluxes is evaluated by analyzing one-dimensional heat and salt budgets of the upper ocean at the moorings and comparing them to the local air–sea fluxes. It is shown that oceanic lateral fluxes converge heat and salt into the formation region during winter thus offsetting the heat loss to the atmosphere and influencing the formation of EDW. A comparison with results from a one-dimensional model shows that without the lateral fluxes EDW would outcrop earlier and it would be colder and fresher. The warm, salty waters transported into the region originate from the Gulf Stream and this suggests that frontal processes likely play a fundamental role in EDW formation and its evolution.

© 2013 Elsevier Ltd. All rights reserved.

1. Introduction

Eighteen Degree Water (EDW), the subtropical mode water (STMW) in the North Atlantic, was first given its name by [Worthington \(1959\)](#) and is observed to the south of the Gulf Stream (GS), as a weakly stratified water mass with temperature of $\sim 18^\circ\text{C}$ and salinity of ~ 36.5 . It forms every winter, when it outcrops to the surface, and resides beneath the mixed layer for the rest of the year. EDW is particularly important for the region since it integrates the effects of both oceanic advection and atmospheric forcing over multiple years ([Kelly et al., 2010](#)). Thus, an accurate understanding of EDW formation and destruction is essential to the description of the air/sea climate of this large region. Yet, controversy exists regarding its annual formation rate. Based on the traditional paradigm that EDW is formed locally due to the strong air–sea interaction near the frontal region ([Worthington, 1959](#); [McCartney, 1982a, 1982b](#); [Talley and Raymer, 1982](#)), [Speer and Tziperman \(1992\)](#) estimated an annual

formation rate of EDW of 15 Sv using an air–sea flux integration scheme by [Walin \(1982\)](#). A notably different number (5 Sv) was instead estimated by [Kwon and Riser \(2004\)](#) from subsurface float observations. Possible causes for this discrepancy include uncertainties in the air–sea flux forcing, a more complex and non-local formation process as well as the specific definition of EDW used in each study ([Joyce, 2011a, 2011b](#)). One likely player leading to this discrepancy is the lateral, diabatic exchange through the mixed layer (ML) facilitated by mesoscale eddy processes, which play an order one balance in the buoyancy budget ([Marshall, 2005](#)). A related controversy exists on the formation region. [Maze et al. \(2009\)](#) recently conclude that EDW can be formed by air–sea heat fluxes in the northern Sargasso Sea, from $\sim 30^\circ\text{N}$ to just south of the Gulf Stream. [Joyce et al. \(2013\)](#), on the other hand, propose a non-local formation paradigm, in which 50%–90% of the new EDW can be formed at the GS, instead of in the Sargasso Sea, and argue that the EDW found in the northeastern Sargasso Sea is mainly advected into this region from the GS. These contrasting views indicate that our understanding of the formation and evolution of EDW is still limited.

Here we use observation data from two subsurface moorings, deployed in the EDW outcropping region, just south of the GS, for ~ 1 year, to investigate the process of EDW formation and

* Correspondence to: Physical Oceanography Department, Woods Hole Oceanographic Institution, Clark 344b, MS#21 Woods Hole, MA 02543
Tel.: +1 508 289 2404; fax: +1 508 457 2181.

E-mail address: xdavis@whoi.edu (X.J. Davis).

evolution as part of the CLIVar MODO Water Dynamics Experiment (CLIMODE; The CLIMODE Group, 2009). We use these data to address the following questions: (1) Does EDW form at the mooring locations? (2) What role do lateral oceanic processes play in EDW formation? (3) What is the relative importance of advection compared with the atmospheric forcing in the EDW evolution?

The paper is organized as follows. The subsurface mooring data from CLIMODE, the auxiliary air–sea surface flux data used and the analysis method are described in Section 2. In Section 3, we describe the observed EDW in detail, including its seasonal evolution and water mass property variations. The high frequency lateral advection observed in the mooring record, their influence on the EDW formation and properties are addressed in Section 4. In Section 5, we summarize our results.

2. Data

2.1. Mooring data and its processing

Two subsurface moorings C and D were deployed from November 2005 to November 2007, with mooring turn-around in November 2006 just south of the GS (Fig. 1) at locations C (38.38°N, 55.86°W) and D (36.09°N, 60.17°W). These two mooring sites are at the gate of subduction (where the subduction mainly occurs) and these observations were designed originally to study the EDW subduction. However, as discussed later, the mooring record was dominated by high frequency signals. Both moorings were equipped with profiling instruments (McLane Moored Profilers, MMPs) that measured temperature, conductivity and velocity from 100 m to ~630 m, and 300 kHz ADCPs (Acoustic Doppler Current Profilers) which measured velocity from a depth of 100 m to the surface. Moored CTD (Conductivity, Temperature, Depth) sensors and current meters, deployed just above and below the MMPs, slightly extended the MMPs' record (See Table 1 for instrument and sampling period). MMPs profiled every ~6 h during year 1 and ~9 h during year 2. During the first year (November 2005–November 2006), both moorings

suffered blow-downs of up to 600 m (due to GS encroachment and/or strong eddies), which caused mechanical failure of both MMPs after approximately three months. In the second year, (November 2006–November 2007), on the other hand, data return was almost 100% and the moorings experienced only limited blow-downs, especially at C (Fig. 2), which is closer to the GS. A detailed description of the data can be found in the technical report (Lund et al., in preparation).

For the purpose of the analysis conducted here we create a time series of properties of potential temperature (temperature, hereafter) and salinity with depth at each location, by merging together data from the different instruments and interpolating on a daily, 4 db vertical resolution grid (Figs. 2 and 3). Because the top of the subsurface mooring was located at approximately 100 m to avoid trawling and even more severe blow-downs, we do not have measurements of temperature and salinity from the surface to 100 m (Table 1). For some of the analysis described below we extend our grid to the surface in two different ways. In method 1, the sea surface temperature (SST) from the NOAA Optimum Interpolation Sea Surface Temperature (OISST, www.ncdc.noaa.gov/oa/climate/research/sst/oi-daily.php, Figs. 2 and 3a) is used to provide surface temperature values. When SST is between 17 °C and 19 °C and moorings are not experiencing a blow-down (i.e. outside of the shaded time periods in Figs. 2 and 3), the mooring data are extrapolated to the surface using a linear

Table 1
Instrumentation and sampling from the moorings.

Instrument	Actual pressure (db)	Measured variables	Resolution in time & space
ADCP	~100	u, v	30 min
Upper SBE ^a	~100	T, S, P	5 min
MMP ^b	~100–630	T, S, u, v	~9 h & 2 db
Lower SBE ^a	~630	T, S	~9 h
RCM ^c	~632	u, v	1 h

^a SBE is the SeaBird-37 Microcat loggers.

^b is the McLane Moored Profilers.

^c is the Aanderra current meters.

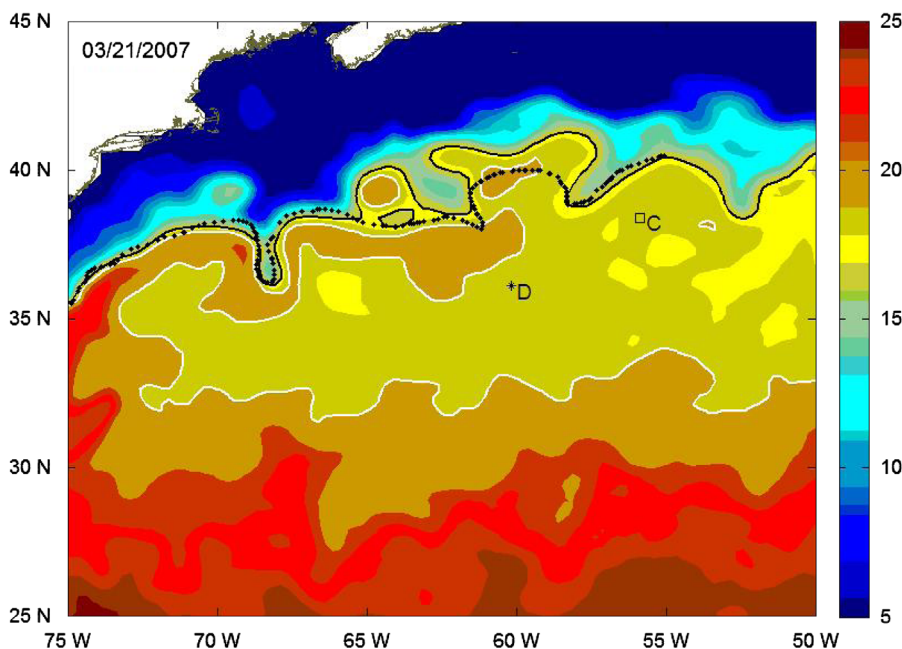


Fig. 1. Locations of the subsurface moorings, C and D, overlaid on the satellite SST (°C) on March 21st 2007 from OISST. The black and white lines are the 17 °C and 19 °C isotherms respectively. The black dashed line is the north wall of the Gulf Stream calculated based on satellite SST-based US navy analysis (Joyce, 2011a, 2011b).

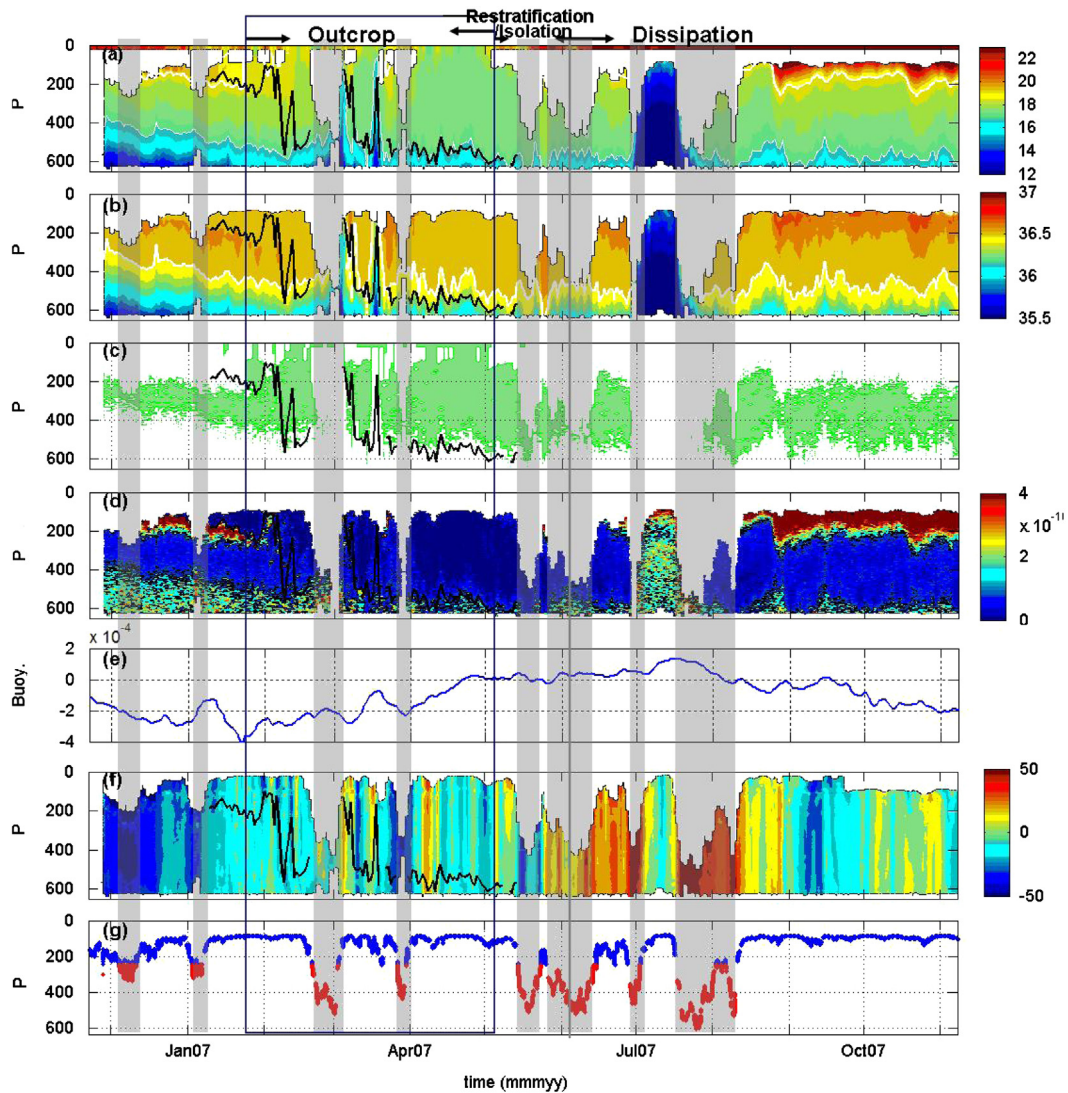


Fig. 2. Temporal evolution of the water properties and corresponding atmospheric forcings at mooring C. (a) Potential temperature (temperature hereafter, °C), (b) Salinity, (c) EDW layer (green shading), (d) Potential vorticity (PV, $\text{m}^{-1}\text{s}^{-1}$), (e) Buoyancy gain from the atmosphere ($\text{kg m}^{-1}\text{s}^{-3}$), (f) Zonal velocity u (cm s^{-1}), (g) Pressure (db) measured by upper SBE. The grey shaded time periods correspond to mooring blow downs in excess of 250 db. The dark grey frame denotes the EDW outcropping period; the grey line divides the restatification (isolation) and dissipation periods (see the text for the description of each period). The black thick lines indicate the mixed layer depth in (a–d) and (f). In (a), the thick and thin white lines are the 19 °C and 17 °C isotherms. In (b), the thick white line is the 36.5 salinity contour. (a and c) are based on MDATAwSST and the rest of the panels use MDATA. (For interpretation of the references to color in this figure legend, the reader is referred to the web version of this article.)

fit between SST and the shallowest moored temperature record. This extended time series (MDATAwSST, hereafter) thus provides a measure of the temperature of the upper 100 m during the period of EDW outcrop and will be used to study the evolution and properties of EDW. Still, salinity data for this layer are not available. A second time series, MDATAwML, will be used to estimate the depth-integrated heat and salt content over the upper ocean. To generate this time series we make the assumption that for the time period when the mixed layer is deeper than the shallowest depth of the mooring observation, as diagnosed by mixed layer properties and no stratification, the temperature and salinity of the upper 100 m are homogeneous and equal to those observed by the uppermost instrument. Thus this second record covers the entire upper part of the water column (0–630 m) only when the mixed layer was deeper than the uppermost part of the mooring. To differentiate from the two ‘extrapolated’ time series, the time series based on the moored data alone is referred to as MDATA.

Because of the mechanical failures of the profilers in the first year, we only focus on the period from November 2006 to November 2007. Periods of blow-down during the second year, indicated in Figs. 2–4, are omitted from our calculations.

2.2. Air–sea flux fields

The turbulent fluxes used in this study were computed using the COARE v3.0 algorithm, QuikSCAT wind speeds, the NOAA OISST sea surface temperature product, and ECMWF analyses for the remainder of the input variables (details can be found at kkelly.apl.washington.edu/projects/climode/index.html). The short and long wave radiation is from the International Satellite Cloud Climatology Project (ISCCP, isccp.giss.nasa.gov/). Precipitation data comes from Global Precipitation Climatology Project (GPCP, www1.ncdc.noaa.gov/pub/data/gpcp/). The spatial resolution of the radiative heat flux and the precipitation data is $1^\circ \times 1^\circ$; while that of the turbulent fluxes and the QuikSCAT wind speed is $0.5^\circ \times 0.5^\circ$. The temporal resolution for all the air–sea

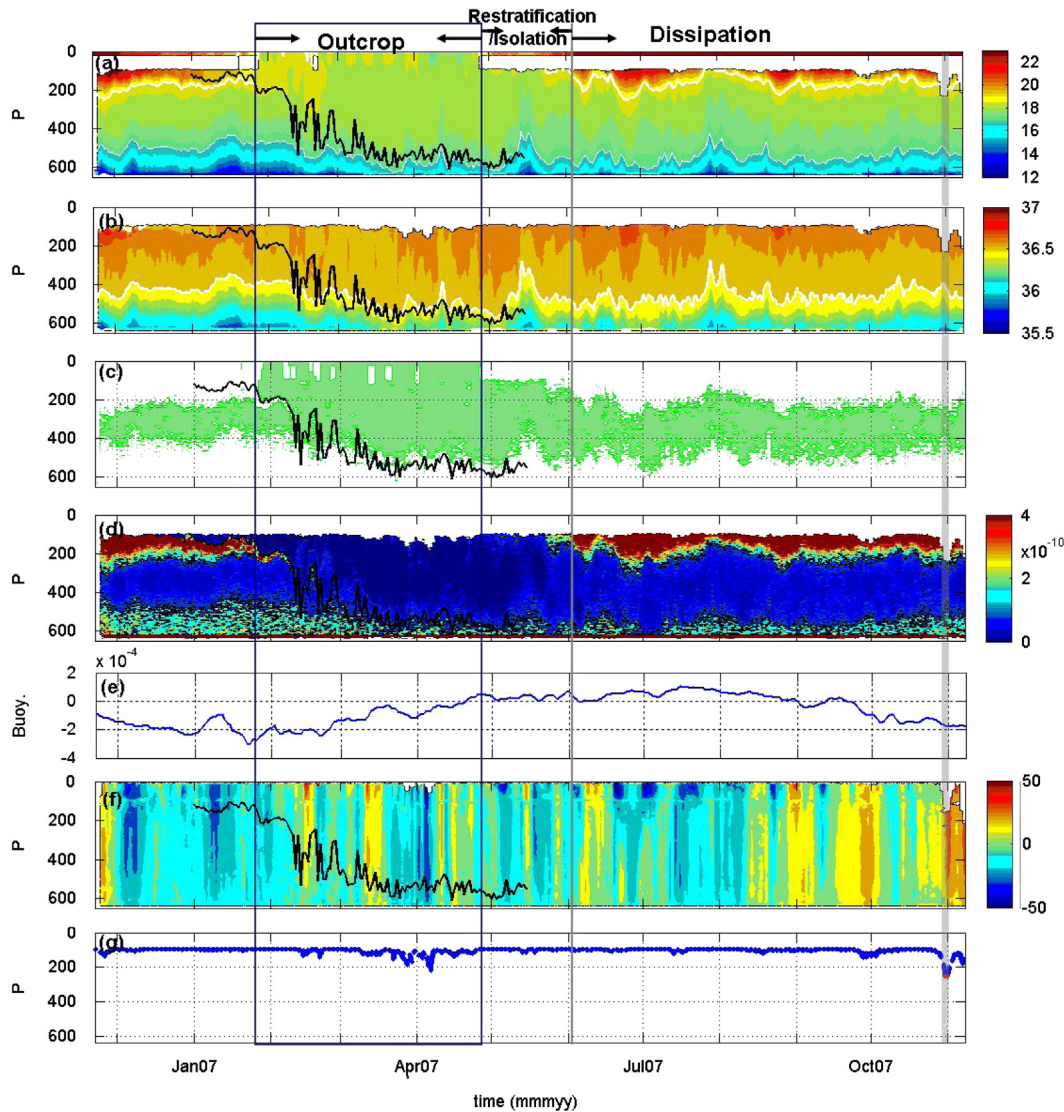


Fig. 3. Same as Fig. 2, for mooring D. (For interpretation of the references to color in this figure legend, the reader is referred to the web version of this article.)

fluxes is daily. The biases for the above mentioned heat fluxes are estimated to be -30 (latent), -10 (sensible), 6 (short wave) and -10 (long wave) W/m^2 , respectively, when compared with direct measurements from the CLIMODE surface flux buoy in the upstream GS front (see The CLIMODE Group (2009) for the buoy location). Here the positive (negative) bias means that ocean gains (loses) too much heat compared to the observation. Thus the net heat flux bias is -44 W/m^2 . The estimated error in the mean bias is 9 W/m^2 . That is, the real ocean heat loss can be as much as $44 \pm 9 \text{ W/m}^2$ less than the heat flux indicated.

Using the above heat flux fields, the evaporation rate E is calculated from the latent heat flux data by $E = Q_{\text{lat}}/L$, where Q_{lat} is the latent heat flux, L is the latent heat of evaporation and has a value of $2.5 \times 10^6 \text{ J/kg}$. The surface buoyancy flux B , i.e. buoyancy gain by the ocean from the atmosphere, is obtained by $B = c_w^{-1}g\alpha Q_t - g\beta s(E - P)$, where $c_w = 4187 \text{ J kg}^{-1} \text{ K}^{-1}$ the specific heat of water, g the acceleration of gravity, $\alpha = -\rho^{-1}\partial\rho/\partial T$ the thermal expansion coefficient, Q_t the net heat gain from atmosphere to the ocean (i.e. downward positive), $\beta = \rho^{-1}\partial\rho/\partial s$ the haline contraction coefficient, E and P are the evaporation and precipitation rates respectively (Gill, 1982). The coefficients α and β are calculated based on McDougall (1987) by employing satellite SST and by assuming a constant surface salinity value of 36.0, which has a minor

impact considering density is more sensitive to temperature than salinity changes in this region. The heat and buoyancy fluxes time series at the two mooring locations are obtained by interpolating the gridded flux products to mooring locations.

3. EDW observed from the mooring

3.1. Definitions of EDW, its outcrop and associated mixed layer depth

In this paper, EDW is defined as a water mass with temperature between 17°C and 19°C and a weak stratification such that $dT/dz \leq 0.006^\circ\text{C/m}$ (Kwon and Riser, 2004). (The weakly stratified layer based on the vertical temperature gradient criterion approximately corresponds to a layer with potential vorticity (PV) smaller than $1 \times 10^{-10} \text{ m}^{-1}\text{s}^{-1}$.) The outcropping time period of EDW, defined by the presence of EDW at the surface, is marked by the dark grey frame in Figs. 2 and 3. During each winter, EDW is renewed (Worthington, 1972, 1976) and the EDW properties are modified by the surface flux along its outcrop. The mixed layer depth (MLD) is defined as the shallowest depth where the vertical gradient of the density is greater than 0.006 kg/m^4 (Dong et al.,

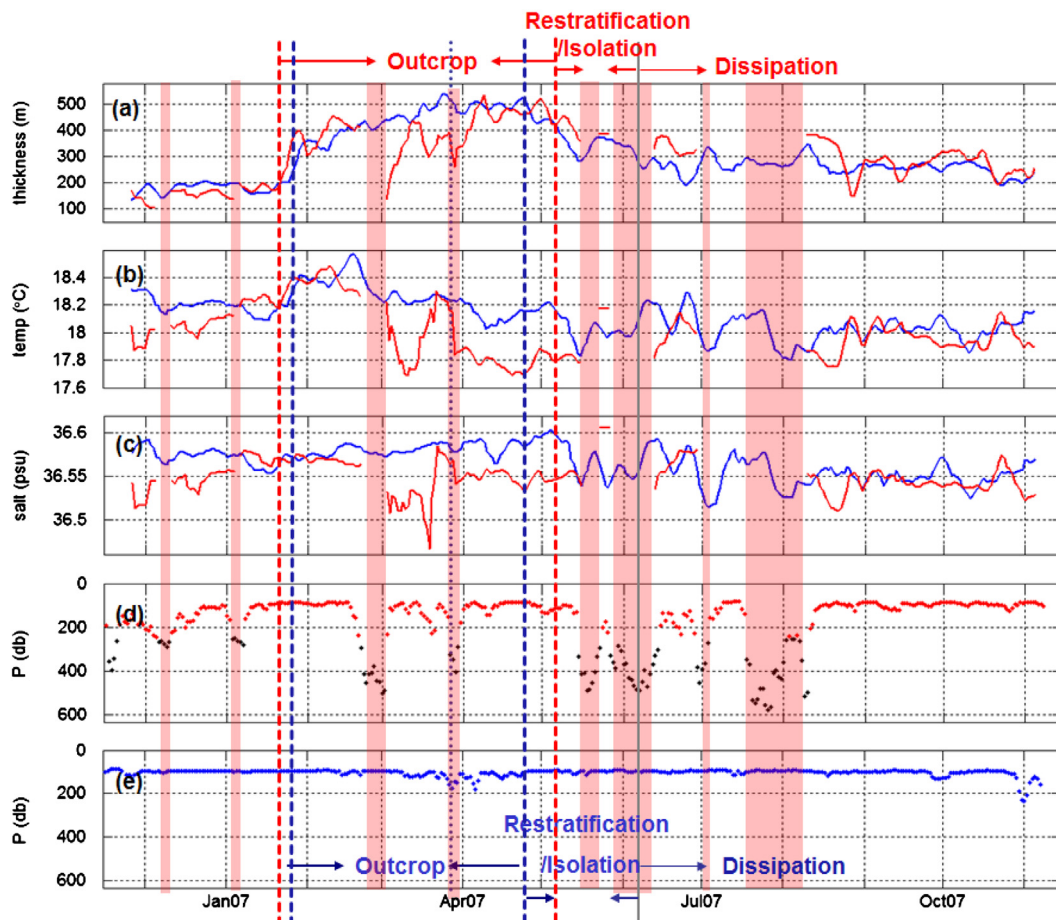


Fig. 4. Properties of EDW: (a) Thickness (m), (b) Mean temperature ($^{\circ}\text{C}$) and (c) Mean salinity of EDW at C (red line) and D (blue line) from November 2006 to November 2007. Pressure (db) measured by the upper SBE at (d) C and (e) D are also shown. The black dots in (d) and (e) indicate mooring blow-downs in excess of 250 db, and these periods are shown as light red shaded areas for C. The red (blue) dashed lines mark the EDW outcropping periods at C (D). The grey line divides the restratification (isolation) and dissipation periods, which occur at approximately the same time for both moorings. (a and b) are calculated based on MDATAwSST and (c) uses MDATA. (For interpretation of the references to color in this figure legend, the reader is referred to the web version of this article.)

2008; Holte and Talley, 2009). During the time of severe mooring blow-downs (when the upper floatation was blown down more than 250 mb; see Figs. 2 and 3g), the MLD is unknown.

3.2. Annual cycle of EDW

EDW is present throughout the observational record at both mooring sites with the exception of a period in July, at C, when a cold, fresh eddy transits past the mooring (Figs. 2 and 3a–d). EDW is a homogenous water mass, with PV values less than $1 \times 10^{-10} \text{ m}^{-1} \text{ s}^{-1}$ (Figs. 2 and 3d), comparable to those observed near Bermuda (Talley and Raymer, 1982; Joyce et al., 2000). This weakly stratified layer is thicker during formation/outcropping season and thinner during the rest of the year. During outcrop, the thickness of EDW is as large as 564 m at mooring D (Fig. 4a), a larger value than that estimated for 1961–2000 using the World Ocean Database 2001 and from profiling floats in this region (Kwon and Riser, 2004; Peng et al., 2006).

The annual cycle of the EDW can be described with three distinct phases: the formation/outcropping (formation, hereafter), restratification/isolation (restratification, hereafter), and dissipation, as suggested by Davis et al. (2011) for the North Pacific STMW (Figs. 2–4). The thickening of the EDW layer in late January is preceded by several months of buoyancy loss and is accompanied by the outcropping of the 19°C isotherm (Figs. 2 and 3e). The formation period is followed by rapid restratification near the surface (Figs. 2 and 3a), during which the outcrop area decreased until it disappeared, and a

fast decline in EDW thickness starting around late April/early May (Fig. 4a) when the EDW is isolated from the surface. The restratification period is characterized by a higher PV, and a warmer and saltier surface layer compared to the EDW (Figs. 2 and 3a–d). The start of the restratification coincides with the time when the buoyancy forcing changes sign from loss to gain (Figs. 2 and 3e). After ~ 1 month of rapid decrease, the EDW enters the dissipation phase and its thickness continues to decrease slowly from early June to the end of the record (Figs. 2 and 3c and 4a). Thus, EDW destruction occurs during both the restratification and dissipation phases. The different mechanisms behind the EDW destruction distinguish the two phases. The EDW destruction during the restratification phase is a fast process (Fig. 4a), which is dominated by the seasonal restratification near the surface associated with the air–sea heat exchange. On the other hand, the EDW destruction during the dissipation phase is a slow process (Fig. 4a) and EDW loss is mainly due to oceanic internal mixing in the subsurface. Note that the two isolated moorings could not capture the whole volume change of EDW and the horizontal spreading of the EDW could also contribute to the thickness change of the EDW observed at the mooring sites.

3.3. Outcropping of EDW and its relationship to ML

The measurements show that EDW outcrops at both mooring sites from late January to early May/late April (Figs. 2 and 3). In late fall/early winter and prior to the outcropping, EDW, is found below the ML between 200 and 400 m and is old EDW formed during

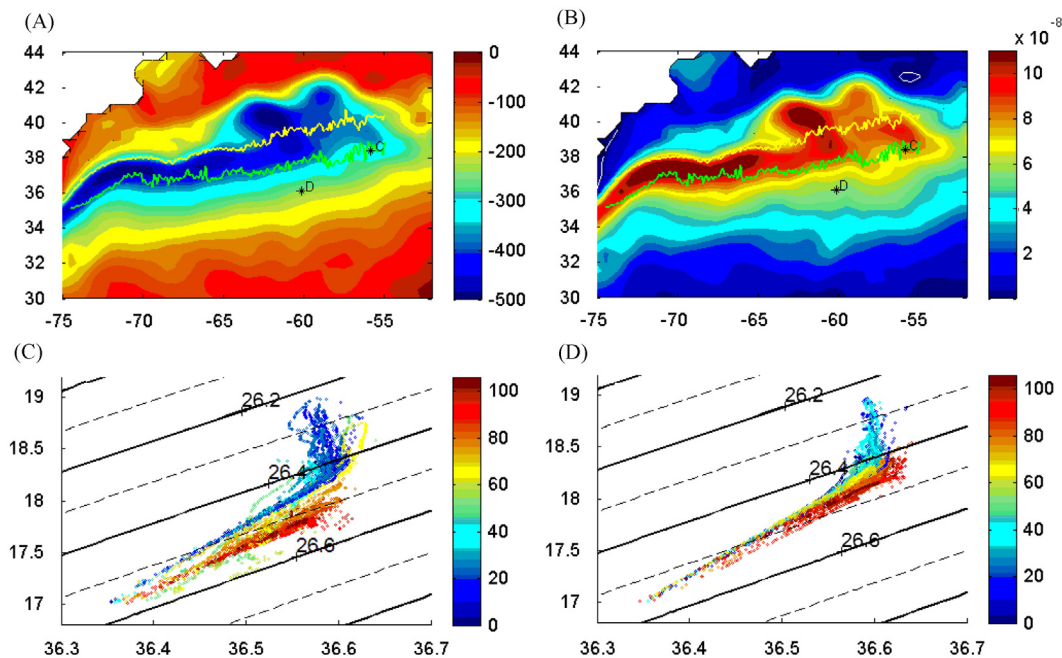


Fig. 5. (A) Net mean heat flux (W m^{-2}) and (B) Mean $E-P$ (m s^{-1}) between January and April 2007. The green and yellow lines indicate the mean position of the south and north walls of the Gulf Stream based on satellite SST-based US navy analysis (Joyce, 2011a, 2011b). The T/S properties of EDW are plotted for (C) mooring C and (D) mooring D from mid-January to end of April, during the outcropping time approximately. The color indicates the time in days starting from January 15th. (For interpretation of the references to color in this figure legend, the reader is referred to the web version of this article.)

previous winters (Figs. 2 and 3c). At the first stage of the outcropping (from the end of January to early February), the ML properties tend toward those of newly formed EDW near the surface. The new surface EDW is separated from the old subsurface EDW by a highly stratified layer with high PV (Figs. 2 and 3c and d). This high PV layer is near the base of the ML; thus ML acts as a divider between the new surface EDW and old subsurface EDW. These two EDW layers coexist only briefly (~ 5 days) at C but longer at D. Shortly thereafter, in the 2nd stage (from early February to mid-March), the ML exhibits large fluctuations as it rapidly penetrates into the old subsurface EDW layer and causes the surface and the subsurface EDWs to mix. MLD fluctuations persist until mid-March, with larger amplitudes at C (~ 400 m) compared to D (~ 250 m). During this time, the new EDW and old EDW are not fully mixed yet, EDW is found both above and below the MLD. The lower boundary of EDW deepens in this stage and may indicate the local formation of EDW. In the last stage (from mid-March to early May/end of April), the ML is deep at both moorings for about 1.5 months and it is filled with homogeneous EDW. At both locations, the winter ML penetrated beyond the existing EDW, thus forming a distinct and thicker EDW.

We note that it is not clear from the observed mooring records alone whether the outcropping of EDW is predominantly due to local 1-D processes or if the observed EDW is advected laterally into the mooring locations, especially considering significant velocities observed (Figs. 2 and 3f). We will further discuss this issue in the following sections.

3.4. Atmospheric forcing and EDW property variations

The mean properties of EDW such as thickness, temperature and salinity at each day are calculated (Fig. 4a–c) and the seasonal evolution of these properties will be discussed together with the overlying atmospheric forcing. Note that only the EDW properties during the non-blow-down time period are plotted (Fig. 4d, e, periods with shading indicate blow-down time spans). The winter atmospheric forcing over this region is characterized by maximum heat

and freshwater loss over the GS and decaying fluxes away from it to its south, where the moorings were located (Fig. 5A and B). In particular, evaporation dominates precipitation at both mooring sites (Fig. 5B). Seasonally, the ocean loses heat (buoyancy) to the atmosphere from late September to late April (Figs. 2 and 3e) and then gains heat during the rest of the year. In the winter of 2007, the heat loss and the freshwater loss were both significantly larger than the mean winter fluxes over previous 19 years (Joyce, 2011a, 2011b).

During outcropping, EDW is exposed to the atmosphere, and the ocean continues to lose a large amount of heat to the atmosphere (at times in excess of 1000 W m^{-2}). We note, however, that at both mooring locations, the outcropped, surface EDW initially warms in late January (Fig. 4b). This warming is likely a result of lateral input of warm anomalies, which offsets the large winter heat loss (assuming that the impact of vertical entrainment from below the EDW is negligible and, in any case, should have the opposite sign). After outcropping, the vertically averaged temperature of EDW at both locations does not follow a monotonic trend (Fig. 4b). For example, the EDW temperature increased in the middle (end) of February at mooring C (D). This suggests that relatively warm waters must be transported to both mooring locations by lateral advection both during and after the winter outcrop.

The mean evaporation minus precipitation ($E-P$) during outcrop is $3.9(2.8) \times 10^{-8} \text{ m s}^{-1}$ at C (D). With atmospheric forcing alone, EDW should become saltier at both locations. However, a salinity decrease is observed at both locations, for example, during March at C (red line in Fig. 4c) and in mid-April at D (blue line in Fig. 4c). During the dissipation periods, the EDW is isolated from the atmospheric forcing, but its temperature and salinity still exhibit clear variations (Figs. 2–4), which is also indicative of lateral oceanic processes.

3.5. Difference of EDW T/S properties between C and D during winter 2007

We compare the EDW evolution at C and D by considering the evolution of its T/S properties (Fig. 5C and D) during the outcrop. These T/S properties show that waters in the EDW range become

progressively colder and collapse towards a unique EDW type, at the end of winter, consistent with the large heat loss to the atmosphere. On the other hand, the salinity range of EDW does not change much through the course of winter. At D, the salinity increases slightly (~ 0.05), consistent with the net evaporation discussed earlier (Figs. 4c and 5d), while at C it decreases slightly (Fig. 5c) even though again we expect evaporation to dominate (Fig. 5b). We attribute this to the cold, fresh events that occur in March at C (Fig. 2a and b and red line in 4c) and note that these may be due to the cross frontal mixing of freshwater found north of GS described in Joyce, 2011a, 2011b. At both C and D locations, the standard deviation (STD) of the EDW salinity increase from January and reaches its maximum in March during the outcrop, which further indicates the intrusion and mixing of new water. After the outcrop, especially during the dissipation phase near the end of the year, the STD is relatively small at both locations. Compared to location C, the STD of EDW salinity at D is much smaller even in the outcropping periods, indicating less intrusion of new water at D.

The deepening of the ML towards the end of the outcrop period at both locations (Figs. 2 and 3b) will contribute to mixing fresher waters from below and drive a decrease in the salinity of the EDW. At C location, the EDW temperature decrease over the winter season is more than that at D (Fig. 5c and d). This larger temperature decrease at C is a likely result of both the larger heat loss (Fig. 5a) and the cold events during March at this location.

In summary, the EDW near the GS (at mooring C) is fresher and cooler than that away from the GS (at mooring D) during outcropping (Fig. 4b and c). Also, the EDW T/S properties at C exhibit greater variability than at D (Fig. 5c and d) which is likely due to the proximity of the GS. Indeed, C was within the GS $\sim 30\%$ of the outcropping time (not shown), while D was south of the GS always based on the GS position from the satellite SST-based US navy analysis (Joyce, 2011a, 2011b). As a result, not only is the atmospheric forcing stronger at mooring C, but the impact of GS meanders is also stronger.

4. Lateral oceanic processes and their effect on ML and EDW

4.1. High frequency variations and eddy-like features observed

At our mooring sites, eddy-like features are observed in the form of high frequency variations of velocity and temperature (Fig. 6a and b). To highlight the eddy activity, the background current, which is calculated as the 31-day running mean of the velocity at each depth, was removed from the observed velocity. The background flow is mostly toward southwest, indicating a source of warm and salty water from GS to the mooring sites (not shown). The residual current shows frequent reversals, which are dominated by mostly barotropic (over the upper 632 m) variability over periods of O (10 days) (Fig. 6a). We speculate that these are due to anti-cyclonic or cyclonic eddies (eddies here are defined as closed circulations), or GS meanders passing by the mooring location. However, the periods when the mooring C experienced blow-downs, e.g., late February to early March, from late May through June and from late July to early August, are primarily due to the GS meanders according to the satellite SSH maps. Therefore, the observations are not sufficient to clearly separate the impact of eddies from that of the meanders at C. And as discussed below, the results shown favor the dominant role of eddies as opposed to GS meander. Of course, the mooring D would not experience the GS meandering. This statement is supported by considering the temperature anomalies at D at fixed depths, where the anomaly is defined as the difference between the original data and a 31-day running mean low-pass filtered time

series at each depth (Fig. 6b), and showing that these temperature anomalies are associated with reversals in meridional velocity, as one would expect from a passing eddy (Fig. 6a and b). Similar events occur at C (not shown).

An in-depth analysis of the eddy characteristics at the two isolated mooring sites is beyond the scope of this study. However, we can calculate the eddy characteristic time scale from the autocorrelation of the temperature and velocity anomalies (Fig. 6e and f). These results show that eddies are coherent with depth and have a characteristic time scale of ~ 10 days at D, i.e. it takes ~ 10 days for eddies to pass the mooring site D. At mooring C, this time scale is a little longer, ~ 14 days (Figure not shown), but less robust due to frequent data gaps. These estimates are consistent with previously reported values for the eddy characteristic time scale in the region of interest (Veneziani et al., 2004).

The eddy kinetic energy (EKE) is also calculated at both mooring sites (red lines in Fig. 6c and g) based on the velocity anomaly (upper 250 m mean) discussed earlier. Despite the missing data during blow down time periods at C, it is still clear that EKE is much larger (as much as $1418 \text{ cm}^2/\text{s}^2$) than that at D (maximum EKE is $587 \text{ cm}^2/\text{s}^2$). With the use of satellite SSH data, the geostrophic velocity and EKE is obtained (blue lines in Fig. 6c, d and g). Compared to the EKE observed by the mooring, the EKE from satellite data is much smaller at D; At C, the maximum EKE from satellite occurred during July, when a cold core eddy passing by (Fig. 6g). At both mooring locations, the EKE from satellite does not fully resolve the high frequency features as that from mooring data. A comparison between the full velocities calculated from SSH (geostrophic, blue line in Fig. 6d) and from mooring observations (upper 250 m mean, red line in Fig. 6d) reveals a similar low frequency variability between them, but SSH does not resolved the high frequency variations recorded by the moorings (Fig. 6d). As the autocorrelation indicates, eddies take ~ 10 days to pass the moorings and these eddies cannot be fully resolved by the 7-day merged satellite product. The spectrum of EKE at D also exhibits a significant peak at ~ 10 days.

Still, the satellite SSH data offers a valuable resource for tracking eddy activities; for example, it can be seen from satellite image that from July 2nd to July 21st, mooring C was inside a cold core eddy, which traveled toward southwest first and then back to northeast (Figure not shown). This cold core eddy has a diameter of ~ 170 km, carries cold water to the mooring C location, which corresponds to the cold anomaly observed in the temperature record during July (Fig. 2a). However, most of the eddy-like features observed in the mooring locations, especially at D, cannot be traced in the satellite SSH data. The possible causes can be that the sizes of the eddy-like features observed are smaller than the satellite spatial resolution, and/or the short-time passing, i.e. ~ 10 days, of these eddy-like events are not resolved by the satellite.

Next we consider the impact of these fluctuations on the upper ocean temperature (vertically averaged over upper 610 m, $T_{mean} = (1/610) \int_0^{610m} T(z) dz$, Fig. 7A) at D using MDATAwML (C exhibits a similar behavior and is not shown here). The upper ocean cools more than 1°C from November to late January at mooring D, at which point the ML deepens rapidly and the temperature remains at $\sim 18^\circ\text{C}$ with small variations (Fig. 7A). On daily time scales, however, changes in the upper ocean temperature exhibit high frequency variations that are associated with the high-frequency velocity fluctuations (Fig. 7B). The magnitude of these changes is as much as 0.4°C over the entire layer which, in turn, is consistent with those shown in Fig. 6b. If we estimate the surface heat that would be necessary to account for these changes, $Q_{total} = 610\rho C_p(\Delta T_{mean}/\Delta t)$ (where $\Delta t = 1$ day), this is on the order of 10^4 W/m^2 , i.e. an order of magnitude larger than the estimated net surface heat flux (Q_{net} , Figs. 8 and 9B) at

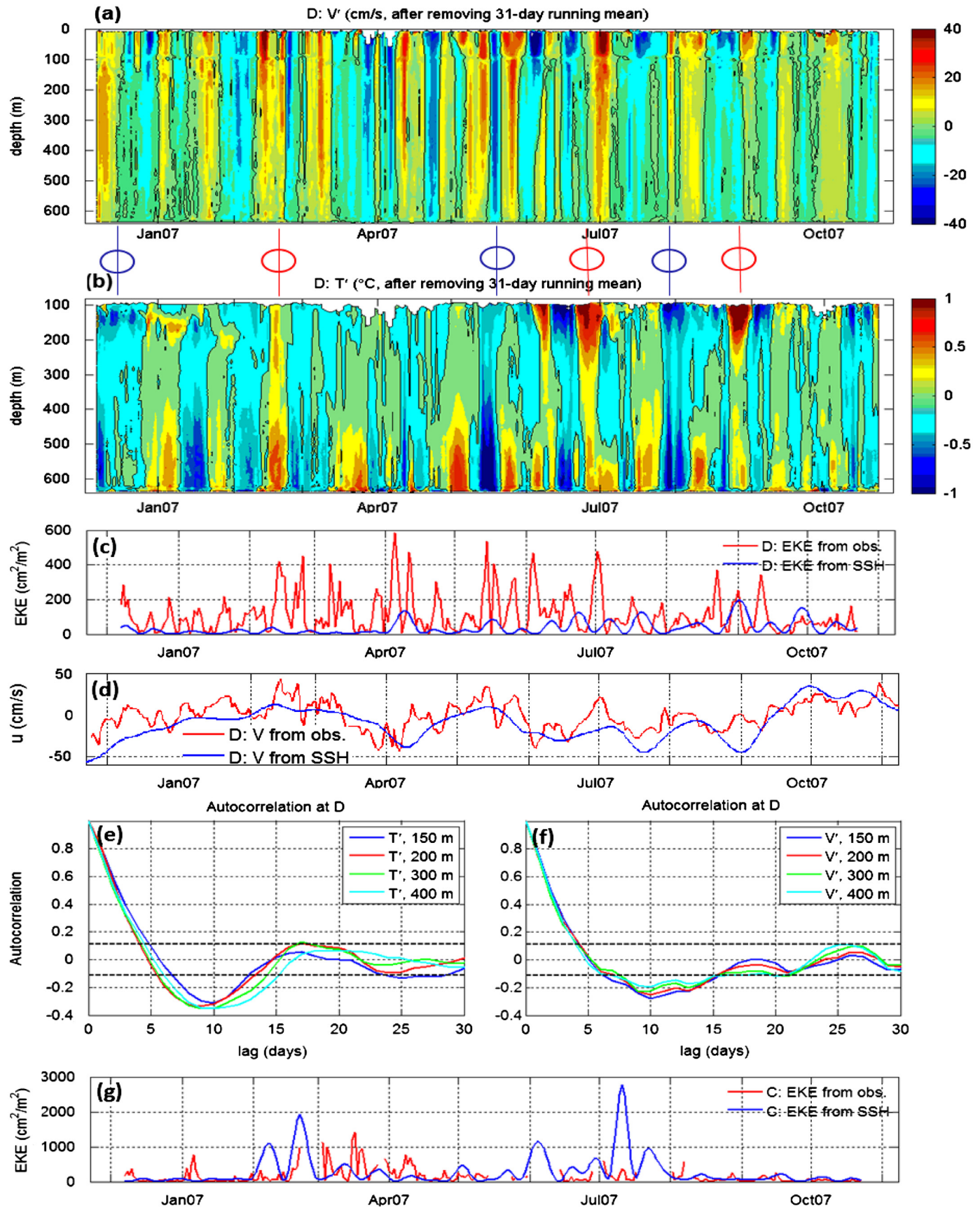


Fig. 6. (a) Meridional velocity anomaly V' (cm s^{-1}) and (b) temperature anomaly T' ($^{\circ}\text{C}$) (the anomalies are the original data minus 31-day running mean) (c) the EKE (d) full meridional velocity (31 day running mean plus anomaly) (e) autocorrelation of temperature anomalies and (f) velocity anomalies, all at D. (g) is the EKE at C. Red lines in (c), (d) and (g) are based on mooring observations and blue lines are derived from satellite SSH. EKE from observation shown in (c) and (g) are calculated from the mean velocity of upper 250 m. In (d), the velocity from observation is also the mean of the upper 250 m velocity. The red and blue circles between (a) and (b) indicates the warm and cold eddies passing by the mooring, which are indicated by the correspondence between current reversals in (a) and the temperature anomalies in (b) as pointed by the line across the circles. (For interpretation of the references to color in this figure legend, the reader is referred to the web version of this article.)

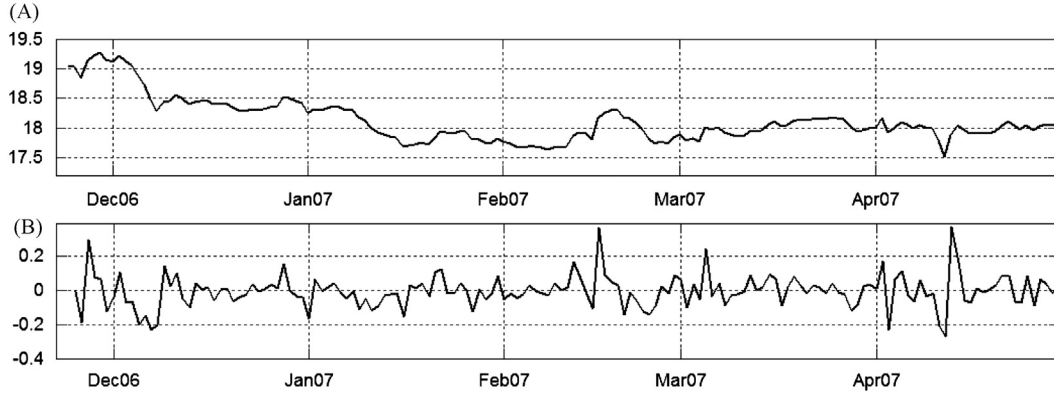


Fig. 7. (A) Mean temperature ($^{\circ}\text{C}$) of the upper 610 m from mooring D. (B) Mean temperature change ($\Delta T/\Delta t$, $^{\circ}\text{C}/\text{day}$) over the upper 610 m with $\Delta t=1\text{day}$. All the calculations here are based on MDATAwML.

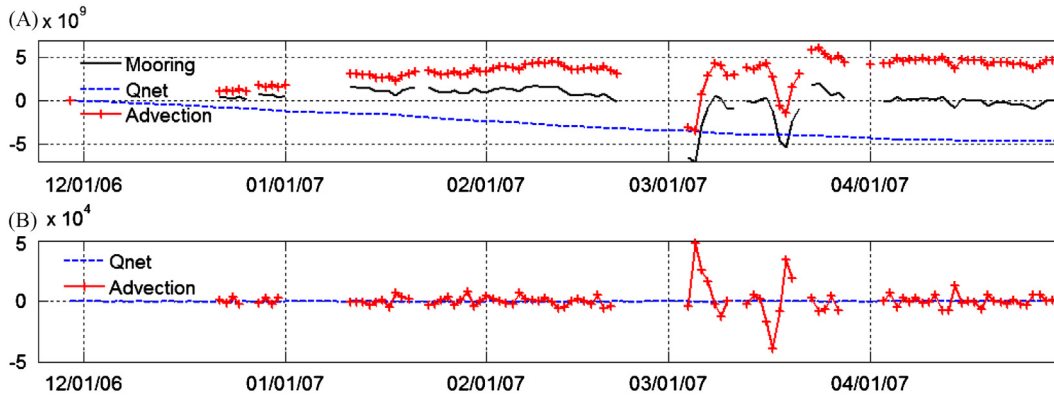


Fig. 8. (A) Cumulative heat content of the upper 632 m heat at mooring C (J/m^2 , see text). The black, blue and red lines are heat contents calculated from the mooring observation ($(HC)_{total} |_{t_0}^t$ from MDATAwML), the integrated net surface heat flux ($(HC)_{Q_{net}} |_{t_0}^t$), and the cumulative residual ($(HC)_{Adv} |_{t_0}^t = (HC)_{total} |_{t_0}^t - (HC)_{Q_{net}} |_{t_0}^t$), respectively. (B) Net surface heat flux (W/m^2 , blue line, Q_{net}) and the implied lateral heat flux (red line, $Q_{Adv} = Q_{total} - Q_{net}$) at mooring C. (For interpretation of the references to color in this figure legend, the reader is referred to the web version of this article.)

any given time during winter. This suggests that these high-frequency variations at both two moorings are likely associated with lateral advection of colder/warmer waters past the moorings, which could be associated with GS meanders or passing eddies.

Though it is challenging to diagnose the cause of these fluctuations using single point measurements, we here make an attempt to establish the role of these lateral events in the formation of the EDW. The main questions that interest us are: (1) What is the relative importance of the lateral fluxes compared to the atmospheric fluxes in the upper ocean heat/fresh water content during EDW formation season? (2) Do these lateral processes facilitate or impede the outcropping (formation) of the EDW? (3) Can we determine the source of these lateral anomalies?

4.2. Relative importance of advection compared to atmospheric forcing: depth-integrated heat and salt budget analysis

As shown above, the high frequency variability of the upper ocean temperature appears to be dominated by lateral advection. To examine the relative importance of advection compared to atmospheric forcing during the season when EDW is formed, we compare the heat content changes observed at the moorings' locations with those expected if the surface fluxes were the only driver. To avoid the large approximately daily fluctuations, we use the cumulative change from the initial time t_0 instead, and the heat content is calculated over the upper 632 m at mooring C (over the upper

610 m at mooring D, $(HC)_{total} |_{t_0}^t = [\rho C_p \int_0^{610\text{m}} T(z) dz] |_{t_0}^t$) (black lines in Figs. 8 and 9A, based on MDATAwML). We compare this with the cumulative surface heat $(HC)_{Q_{net}} |_{t_0}^t = \int_{t_0}^t Q_{net} dt$ (blue lines in Figs. 8 and 9A). Assuming that the vertical entrainment through the lower boundary at 632 m (610 m) is small, the difference between these two quantities must be due to lateral advection, i.e. $(HC)_{Adv} |_{t_0}^t = (HC)_{total} |_{t_0}^t - (HC)_{Q_{net}} |_{t_0}^t$ (red lines in Figs. 8 and 9A). The initial time t_0 is set to be November 29th and December 17th in 2006 at mooring C (D) (before the EDW outcropping and when we have the 1st mooring measurements after the initialization of the PWP model, see Section 4.3 and Figs. 11 and 12), the time t is each day after t_0 until April 30th, 2007 (near the end of the outcropping time and buoyancy switched signs). The corresponding air–sea heat flux Q_{net} and the estimated lateral heat flux $Q_{Adv} = Q_{total} - Q_{net}$ using $\Delta t=1\text{day}$ are also shown (Figs. 8 and 9B).

This analysis shows that the lateral heat flux convergence is substantial and, to a large extent, balances the surface heat loss. The daily lateral heat flux is one order larger than the net air–sea flux (Figs. 8 and 9B). During winter of 2007, the ocean lost heat to the atmosphere continuously until late April (blue lines in Figs. 8 and 9A). This heat loss, however, did not result in a progressive cooling of the upper ocean (black lines Figs. 8 and 9A) which means it was continuously balanced by the cumulative impact of the lateral oceanic convergence of heat, estimated as a residual (red lines, Figs. 8 and 9A). We note that this is an integral effect of the lateral fluxes because on short-timescales these fluctuate rapidly in magnitude and in sign (Figs. 8 and 9B). Yet, our results show that the net effect of the lateral fluxes is to warm

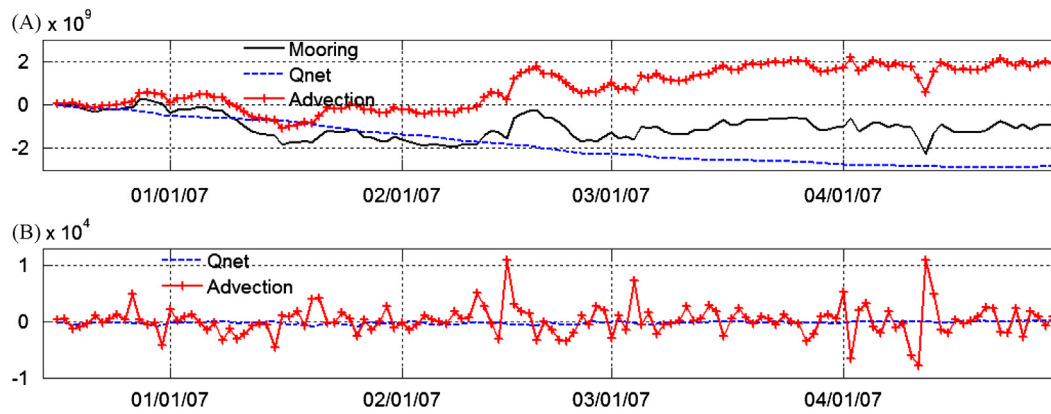


Fig. 9. Same as Fig. 8, except that at mooring D location and heat budget is calculated over upper 610 m. (A) Heat content at mooring D (J/m^2) and (B) Heat flux at mooring D (W/m^2). (For interpretation of the references to color in this figure legend, the reader is referred to the web version of this article.)

Table 2a

Mean heat flux during winter (from November 26 (December 17) at C (D) in 2006 to April 30 in 2007).

Heat flux (W/m^2)	Qnet	Mooring obs.	Advection
Mooring C	-352.2	4.8	357.0
Mooring D	-243.7	-60.0	183.7

Table 2b

Same as Table 2a, except for freshwater flux (where negative advection terms mean the advection of salty water to moorings C and D).

Fresh water flux ($\times 10^{-7}$ m/s)	P-E	Mooring obs.	Advection
Mooring C	-0.39	-1.58	-1.19
Mooring D	-0.34	-1.46	-1.12

the water column indicating that the oscillations largely cancel out and that the result is a mean advection of warm waters into the region. At D, the mean heat flux to the atmosphere during the winter months, $-243.7 \text{ W}/\text{m}^2$, is almost entirely compensated by the mean heat flux due to advection, $183.7 \text{ W}/\text{m}^2$ (Table 2a). At C, the heat loss to the atmosphere is slightly over-compensated by the convergence of heat due to advection, and both values are larger than those at D, probably due to its proximity to the GS (Fig. 9, Table 2a). As described earlier, the upper bound of the heat flux product error is $-44 \text{ W}/\text{m}^2$, whose magnitude is much smaller than that of the mean heat flux -352.2 (-243.7) W/m^2 at C (D). Thus this error doesn't change our result qualitatively.

From a similar analysis on the freshwater flux, we found that the freshwater flux by advection dominates the variability of the upper ocean freshwater content during winter and that the net advection of salty water is an order of magnitude larger than that due to the net evaporation (Table 2b).

4.3. Role of lateral processes in EDW outcropping and properties: PWP model simulation

The 1-D heat and salt budget analysis revealed the importance of the lateral processes in setting the upper ocean temperature and salinity. However, the role of these lateral processes on the EDW formation/outcrop and properties needs further examination since the budget analysis cannot single out the EDW layer. Next, to evaluate the impact of lateral oceanic processes specifically on the EDW formation and its properties, we ran a one-dimensional Price–Weller–Pinkel ML model (Price et al., 1986, hereafter PWP model). We then compare the time of EDW

outcrop and its properties with those observed at C and D. Similarly to the vertically integrated budgets above, we attribute the difference between the model and the data to the impact of lateral processes (primarily advection), which are set to zero in the PWP model calculation. Though it has been argued the mixing in PWP doesn't penetrate as deep as that in the observation in some cases (Large et al., 1994), we note that the PWP model has been successfully used in numerous studies to investigate the ML structure in tropical and subtropical regions (Schudlich and Price, 1992; Plueddemann et al., 1995; Anderson et al., 1996; Ladd and Thompson, 2000; Qiu et al., 2004; Qiu and Chen, 2006) and, in particular, mode water regions in the subtropical gyre of North Pacific (Ladd and Thompson, 2000; Qiu et al., 2004; and Qiu and Chen, 2006). With the aid of PWP, Ladd and Thompson (2000) studied the formation mechanism of Central Mode Water and Eastern Subtropical Mode Water; Qiu et al. (2004) focused on the analysis of the synoptic atmospheric impact on the upper ocean thermal structure at a site of STMW formation. Both of the above mentioned studies ignored advection but indicated that advection might be important. Qiu and Chen (2006) examined the decadal variability of North Pacific STMW using 1-D PWP based on the observation that advection of heat is small during year 1996–2004.

In our simulations, the density and the vertical structure of the ocean are forced by the atmospheric forcing only. Vertical mixing occurs when any of the following criteria are met: (1) the upper ocean has a static instability $\Delta\rho/\Delta z \leq 0$; (2) the ML is unstable, i.e., the bulk Richardson number R_b at the base of the ML is below the critical value 0.65, where $R_b = g\Delta\rho h/\rho_0[(\Delta u)^2 + (\Delta v)^2]$; or (3) there is a shear instability, i.e., the gradient Richardson number $R_g = (g\Delta\rho/\Delta z/\rho_0)/[(\Delta u/\Delta\rho)^2 + (\Delta v/\Delta\rho)^2] \leq 0.25$, where h is the diagnosed ML thickness, $\Delta\rho$, Δu , Δv are the density and velocity difference between the ML and the layer right below, and Δz is estimated as the average thickness of the layers above and below.

Two PWP model integrations were performed with vertical resolution of 2 m to depths deeper than 610 m (sufficient to include the ML throughout the observation period). Each run is initialized with the observed $T(z)$ and $S(z)$ using CTD profiles in late fall (November or December) obtained during the CLIMODE field campaigns (Fig. 10. The CLIMODE Group, 2009) and the forcing used is the daily atmospheric forcing (heat and freshwater) described in Section 2. The model is run from late fall to end of the April after which the ocean switches from a total heat loss phase to a gain phase. The model run at mooring C (D) is referred to as Run C (Run D).

In our 1-D PWP model simulation, EDW outcrops earlier than what is observed (Figs. 11 and 12a–d). This can be explained by considering that EDW outcropping is highly sensitive to the

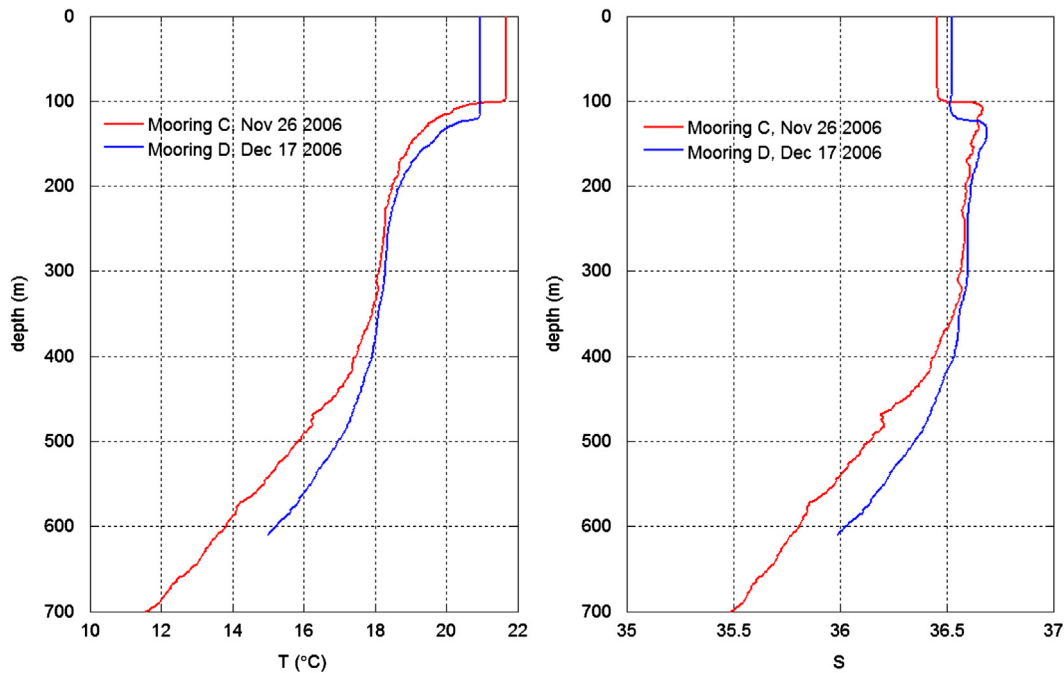


Fig. 10. Observed Temperature (left panel) and Salinity (right panel) at the mooring locations used to initialize the PWP model integrations.

stratification of the upper ocean. In the ‘real’ ocean, we have shown that this is strongly influenced by the lateral advection of warm, salty waters at both locations which increases stratification (throughout the upper ~ 630 m) and delays EDW outcropping compared to the modeled no-lateral flux scenario. After outcropping, the temperature of EDW in the model runs is comparable to that observed for about two weeks (if we take into account the different outcropping times (Figs. 11 and 12f). Eventually, however, the modeled EDW temperatures drop rapidly below the observed temperatures (and well below 17°C in Run C).

In terms of salinity, the modeled EDW salinity at C is also close to the observed value shortly after outcropping, but gradually becomes too fresh (Fig. 11g). In Run D, on the other hand, the observed salinity is comparable to the modeled salinity (Fig. 12g). We attribute this to the fact that in Run C, the mixed layer deepening entrains too much thermocline water into the EDW layer resulting in a colder and fresher EDW. The thicknesses of the modeled EDW are initially different from those observed due to the difference in the outcrop time, but in reasonable agreement after the outcrop (Figs. 11 and 12e). This indicates that lateral advection plays an important role in shaping the EDW properties, and especially its temperature, salinity and timing of the outcrop, by maintaining the stratification and a direct supply of heat and salt. The model–observation differences are larger at C than that at D, which indicates that the role of lateral processes is greater at C than at D, consistent with the closer proximity to the GS.

5. Summary

Two moorings were deployed near the presumed gate of the subduction with the original intention to observe the EDW subduction. However, the mooring record is dominated by high frequency variations as discussed in Section 4.1. Therefore, we focus on the EDW formation, evolution and the role of the high frequency variations in the local heat, salt budget and EDW properties with this data set. EDW is observed throughout the year at both mooring locations, with a maximum thickness of

564 m at D. The EDW at C (closer to the GS) is fresher and cooler than at D. Three distinct phases are observed in the EDW annual cycle: an outcropping period, followed by restratification period associated with rapid loss of EDW near the surface, and a dissipative phase during which EDW loss is mainly through the slower diffusive processes. Outcropping of EDW at both locations starts in late January and ends in late April/ early May, with a slightly earlier start and later ending at C. The beginning of the outcrop period is preceded by a few months of accumulated buoyancy loss and accompanied by a gradual deepening of the ML. The rapid restratification coincides with the time when the atmospheric forcing shifts from buoyancy loss to gain for the ocean and is associated with positive temperature and salinity anomalies near the surface. EDW thickness increases during outcropping and rapidly decreases during restratification. The decrease in thickness continues at a slower rate in the dissipation phase.

Our results suggest that the formation and restratification of EDW is the result of both local atmospheric forcing and lateral advection (assuming the mixing and entrainment below ML is small). The role which the lateral processes play is examined both in terms of one-dimensional depth-integrated heat and freshwater budgets as well as using a one-dimensional model initialized using the observed fall profiles and forced by our best estimate of the air–sea fluxes. Our results indicate that oceanic lateral processes converge warm and salty water into both locations, thus slowing the deepening of the mixed layer and delaying the outcropping (formation) of EDW in early winter. The lateral processes also strongly influence the properties of EDW which, without it, would be much colder and fresher. The cumulative impact of this lateral heat flux convergence by the ocean circulation during winter is shown to be of the same order and of opposite sign of the cumulative surface heat loss. The convergence of salt by the lateral fluxes greatly exceeds the freshwater forcing. Closer to the GS, the role lateral fluxes play in the heat budget can be even larger as revealed by Silverthorne and Toole (2013), in which they performed a quasi-Lagrangian study of the upper ocean heat balance during February and March 2007 using CLIMODE float data.

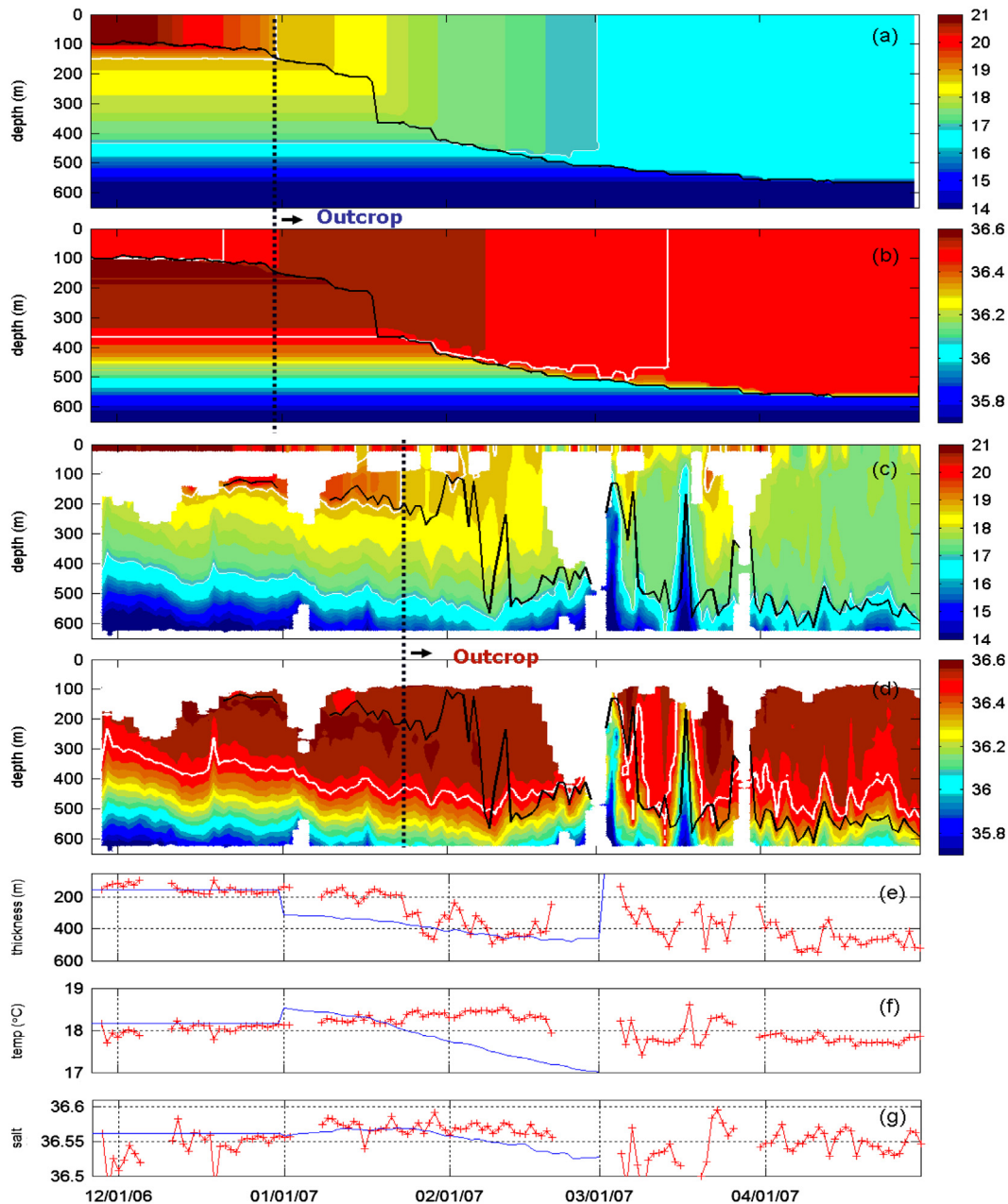


Fig. 11. Comparison between the PWP runs and the mooring observations. (a) Temperature ($^{\circ}\text{C}$) and (b) Salinity in Run C. (c) Temperature ($^{\circ}\text{C}$) and (d) Salinity from the observation at mooring C. (e) EDW thickness (m), (f) mean EDW temperature ($^{\circ}\text{C}$) and (g) mean EDW salinity from Run C (blue solid lines) and the observation at the mooring C (red lines with cross). In (a) and (c), the thick and thin white lines are the 19°C and 17°C isothermal surfaces, respectively. In (b) and (d), the thick white line is the 36.5 salinity contour. The black solid lines in (a–d) indicates the MLD. (For interpretation of the references to color in this figure legend, the reader is referred to the web version of this article.)

Several pieces of evidence suggest that these fluxes are due to eddy fluxes (or/and GS meandering) from the GS into the Sargasso Sea interior. First, the impact of the lateral fluxes is more significant close to the GS than farther away. Second, these fluxes are associated with the convergence of heat and salt and are therefore consistent with a GS source, since its waters are warmer and saltier with respect to the region studied here.

Averaging over many annual cycles, and assuming steady state, the convergence of heat and salt during a year is expected to balance the net heat and freshwater loss to the atmosphere. Interannually, one does not necessarily expect these two to balance exactly which, in turn, gives rise to oceanic heat content variability which is thought to influence climate on longer time scales. Yet, beyond the interannual changes, these results show

that the atmospheric forcing and the ocean heat/salt convergence actually balance during winter, i.e. during the time of EDW formation, thus departing from the traditional paradigm for intermediate/dense water formation regions where net cooling of the water column by the atmosphere in winter is balanced by net warming through the rest of the year (e.g. Straneo, 2006). More quantitatively, if we consider November 2006 to November 2007, the net surface heat loss from the ocean is 5.84×10^9 (3.45×10^9) J/m^2 and the estimated heat convergence by lateral fluxes during winter is 4.78×10^9 (2.13×10^9) J/m^2 at C (D)—i.e. 80 (60) % of the net annual heat loss is balanced by wintertime processes alone. Considering the GS region an air–sea coupled system, the advection of the warm waters into the region during winter time will increase the air–sea temperature difference and

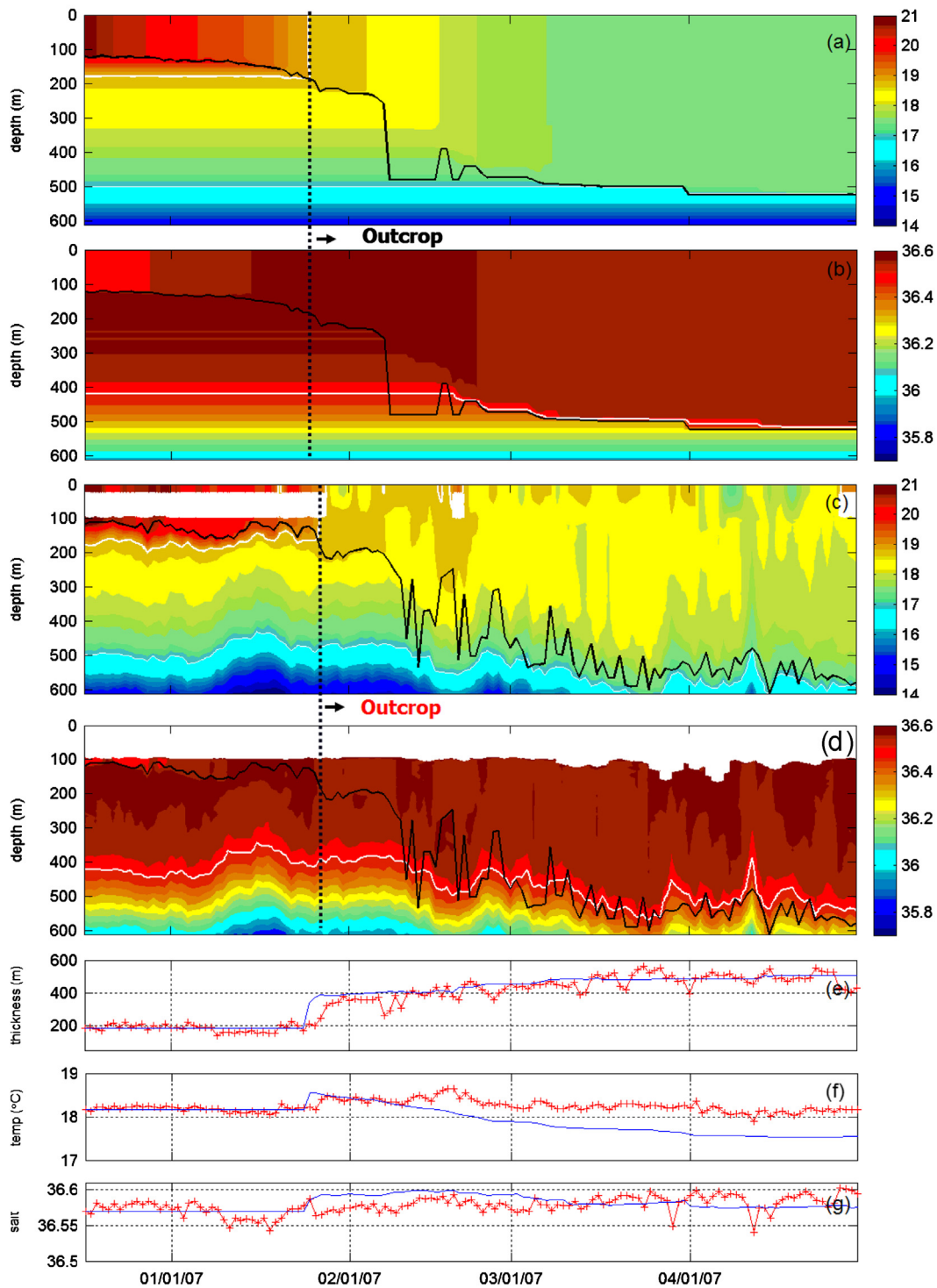


Fig. 12. Same as Fig. 11, except for mooring D. (For interpretation of the references to color in this figure legend, the reader is referred to the web version of this article.)

result in a larger heat flux. Thus, to some extent, the surface fluxes are large because the waters are warm. We note, also, that the GS core temperature has a smaller seasonal cycle compared with the surrounding waters. Thus this larger heat advection in winter is associated with the larger temperature difference between the GS core and the surrounding waters.

The one-dimensional nature of the moored data does not allow us to investigate in depth which lateral processes are responsible for the advection of heat into this region. While the moored data shows plentiful evidence of a very energetic eddy field on a variety of scales (from rings to smaller sub-mesoscale features),

we are unable to determine which scales are actually achieving the heat transport. The high eddy activity in this region, in particular, is exemplified in the finding that the day to day changes in the upper ocean's heat content exceed the magnitude of the atmospheric forcing by one order of magnitude. To a large extent, however, these positive and negative heat anomalies cancel out and it is the residual lateral flux which balances the winter time heat loss.

The picture that emerges from the analysis of these two moored time series is quite different from the classic paradigm of local EDW formation driven by surface heat loss primarily via

one-dimensional convective mixing, followed by export of EDW by mean advection (subduction) into the gyre's interior. Instead, these data show evidence that in the vicinity of the GS at the two mooring sites, which is where EDW outcrops, the formation process is characterized by vigorous interaction/exchange between the GS and the 'interior' outcropping region. This exchange tapers rapidly after the buoyancy loss to the atmosphere ceases due to the fast decrease of the outcrop window, but lasts long enough to account for the rapid restratification. The barotropic nature of these processes also suggests its close tie to the GS low PV water. Because these processes have a large impact on the characteristics of the EDW formed, our results indicate that accounting for them in models is key to a correct representation of mode water formation in the subtropical regions.

The estimates of the lateral fluxes in this study are based on calculating the residual with respect to the surface fluxes and, as such, must take into account the uncertainties in the surface fluxes. The bias for the net air–sea heat flux used is estimated to be $-44 \pm 9 \text{ W/m}^2$ when compared with the direct measurement (the negative bias here means that real ocean loses less heat than that indicated by the air–sea heat flux) from the CLIMODE surface flux buoy in the upstream of GS front (The CLIMODE Group, 2009), which should be considered as an upper bound for the bias at moorings C and D in the interior. This bias is significant, while considerably smaller than the mean $Q_{\text{net}} - 352.2$ (-243.7) W/m^2 at C (D). The interpolation of the satellite flux product to the mooring locations also introduces uncertainties in heat and salt flux. Thus, our evaluation of the lateral advection and its impact are robust, even though, improved heat flux products may help enhance the accuracy of our estimate.

Acknowledgments

We would like to thank many colleagues, technicians, and crew members who helped collect these data and D. Fratantoni, J. Lund, D. Torres (WHOI), in particular. This work has benefited from discussions with T. Joyce, J.J. Park, L. Talley and many other CLIMODE PIs. The PWP used is adapted from the updated version by J.T. Farrar and A.J. Plueddemann. Ms Suzanne Dickinson kindly prepared PWP heat flux forcing field data and provided the flux bias estimates. This work is funded by NSF OCE Grant nos. 0424492 and 0961090.

References

- Anderson, S.P., Weller, R.A., Lukas, R.B., 1996. Surface buoyancy forcing and the mixed layer of the western Pacific warm pool: observation and 1D model results. *J. Clim.* 9, 3056–3085.
- Davis, X.J., Rothstein, L.M., Dewar, W.K., Menemenlis, D., 2011. Numerical investigations of seasonal and interannual variability of North Pacific Subtropical Mode Water and its implications for Pacific climate variability. *J. Clim.* 24, 2648–2665.
- Dong, S., Sprintall, J., Gille, S.T., Talley, L., 2008. Southern Ocean mixed-layer depth from Argo float profiles. *J. Geophys. Res.* 113, C06013, <http://dx.doi.org/10.1029/2006JC004051>.
- Gill, A.E., 1982. Atmosphere–Ocean Dynamics. In: International Geophysics. Series, Vol. 30. Academic Press, 662pp.
- Holte, J., Talley, L., 2009. A new algorithm for finding mixed layer depths with applications to Argo data and Subantarctic Mode Water formation. *J. Atmos. Oceanic Technol.* 26, 1920–1939, <http://dx.doi.org/10.1175/2009JTECH0543.1>.
- Joyce, M., 2011a. New perspectives on Eighteen Degree Water formation in the North Atlantic. *J. Oceanogr.*, <http://dx.doi.org/10.1007/s10872-011-0029-0>.
- Joyce, T.M., Deser, C., Spall, M.A., 2000. On the relation between decadal variability of Subtropical Mode Water and the North Atlantic Oscillation. *J. Clim.* 13, 2550–2569.
- Joyce, T.M., Thomas, L.N., Dewar, W.K., Girton, J.B., 2013. Eighteen Degree Water formation within the Gulf Stream during CLIMODE. *Deep Sea Res.* II 91, 1–10.
- Joyce, T.M., 2011b. New perspectives on eighteen-degree water formation in the North Atlantic. *J. Oceanogr.* 68 (1), 45–52, <http://dx.doi.org/10.1007/s10872-011-0029-0>.
- Kelly, K.A., Small, R.J., Samelson, R.M., Qiu, B., Joyce, T.M., Kwon, Y.-O., Cronin, M.F., 2010. Western boundary currents and frontal airsea interaction: Gulf stream and Kuroshio Extension. *J. Clim.* 23, 5644–5667.
- Kwon, Y.-O., Riser, S.C., 2004. North Atlantic Subtropical mode Water: a history of ocean-atmosphere interaction 1961–2000. *Geophys. Res. Lett.* 31, L19307, <http://dx.doi.org/10.1029/2004GL021116>.
- Ladd, C., Thompson, L., 2000. Formation mechanisms for North Pacific central and eastern subtropical mode waters. *J. Phys. Oceanogr.* 30, 868–887.
- Large, W.G., McWilliams, J.C., Doney, S.C., 1994. Oceanic vertical mixing: a review and a model with a nonlocal boundary layer parameterization. *Rev. Geophys.* 32 (4), 363–403, <http://dx.doi.org/10.1029/94RG01872>.
- Lund, J.M., Davis, X.J., Ramsey, A.L., Straneo, F., Torres, D., Palter, J., Gary, S., Fratantoni, D. CLIMODE Subsurface Mooring Report: November 2005 – November 2007. Woods Hole Oceanographic Institution Technical Report, in preparation.
- McCartney, M.S., 1982a. The subtropical recirculation of mode waters. *J. Mar. Res.* 40, 427–464.
- Marshall, J., 2005. CLIMODE: A Mode Water Dynamics Experiment in Support of CLIVAR. *Clivar Variations*. Spring 2005, vol. 3, no. 2, pp. 8–14.
- Maze, G., Forget, G., Buckley, M., Marshall, J., Cerovecki, I., 2009. Using transformation and formation maps to study the role of air–sea heat fluxes in North Atlantic Eighteen-Degree Water formation. *J. Phys. Oceanogr.* 39, 1818–1835.
- McCartney, M.S., 1982b. The subtropical recirculation of mode waters. *J. Mar. Res.* 40, 427–464.
- McDougall, T.J., 1987. Neutral surfaces. *J. Phys. Oceanogr.* 17, 1950–1964.
- Plueddemann, A.J., Weller, R.A., Stramska, M., Dickey, T.D., Marra, J., 1995. Vertical structure of the upper ocean during the Marine light-mixed layers experiment. *J. Geophys. Res.* 100, 6605–6619.
- Peng, G., Chassignet, E., Kwon, Y.-O., Riser, S., 2006. Investigation of the spatial and temporal variability of the North Atlantic Subtropical Mode Water using float data and numerical model outputs. *Ocean Model.* 13, 65–85.
- Price, J.F., Weller, R.A., Pinkel, R., 1986. Observations and models of the upper ocean response to diurnal heating, cooling, and wind mixing. *J. Geophys. Res.* 91, 8411–8427.
- Qiu, B., Chen, S., 2006. Decadal variability in the formation of the North Pacific Subtropical Mode Water: oceanic versus Atmospheric control. *J. Phys. Oceanogr.* 36, 1365–1380.
- Qiu, B., Chen, S., Hacker, P., 2004. Synoptic-scale air–sea flux forcing in the western North Pacific: observations and its impact on SST and the mixed layer. *J. Phys. Oceanogr.* 34, 2148–2159.
- Schudlich, R.R., Price, J.F., 1992. Diurnal cycles of current, temperature, and turbulent dissipation in a model of the equatorial upper ocean. *J. Geophys. Res.* 97, 5409–5422.
- Silverthorne, K.E., Toole, J.M., 2013. Quasi-Lagrangian observations of the upper ocean response to wintertime forcing in the Gulf Stream. *Deep Sea Res.* II 91, 25–34.
- Speer, K., Tziperman, E., 1992. Rates of water mass formation in the North Atlantic. *J. Phys. Oceanogr.* 22, 93–104.
- Straneo, F., 2006. On the connection between dense water formation, overturning, and poleward heat transport in a convective basin. *J. Phys. Oceanogr.* 36 (9), 1822–1840.
- Talley, L.D., Raymer, M.E., 1982. Eighteen degree water variability. *J. Mar. Res.* 40, 757–775.
- The Climode Group, 2009. Observing the cycle of convection and restratification over the Gulf Stream system and the subtropical gyre of the North Atlantic ocean: preliminary results from the CLIMODE field campaign. *Bull. Am. Meteorol. Soc.* 90, 1337–1350.
- Veneziani, M., Griffa, A., Reynolds, A., Mariano, A.J., 2004. Oceanic turbulence and stochastic models from subsurface Lagrangian data for the northwest Atlantic Ocean. *J. Phys. Oceanogr.* 34, 1884–1906.
- Walín, G., 1982. On the relation between sea-surface heat flow and thermal circulation in the ocean. *Tellus* 34, 187–195.
- Worthington, L.V., 1959. 18 degree water in the Sargasso Sea. *Deep-Sea Res.* 5, 297–305.
- Worthington, L.V., 1972. Anticyclonogenesis in the oceans as a result of outbreaks of continental polar air. In: Gordon, A.L. (Ed.), *Studies in Physical Oceanography—A tribute to Georg Wüst on his 80th birthday*, vol. 1. Gordon and Breach, New York, pp. 169–178.
- Worthington, L.V., 1976. On the North Atlantic circulation. *The John Hopkins Oceanogr. Stud.* 6, 110.